buildings

MDPI

Article

Theoretical Analysis on Thermo-Mechanical Bending Behavior of Timber–Concrete Composite Beams

Bin Guan, Yunchun Dai, Tianyi Zhang, Peng Wu * and Jiandong Zhang *

College of Civil Engineering, Nanjing Tech University, Nanjing 211816, China; binguan@njtech.edu.cn (B.G.); daiyunchun@njtech.edu.cn (Y.D.); zhangtianyi@njtech.edu.cn (T.Z.)
* Correspondence: peng.wu@njtech.edu.cn (P.W.); zhangjd@njtech.edu.cn (J.Z.)

Abstract: In this study, an analytical approach is introduced for predicting the bending behavior of a timber–concrete composite (TCC) beam subjected to a mechanical load and a non-uniform temperature field, in which the orthotropy of timber as well as interfacial slip are taken into consideration. The analytical model addresses the non-uniform temperature field using Fourier series expansion based on the heat transport theory. The stresses and displacements of the TCC beam under the thermo-mechanical condition are governed by the thermo-elasticity theory, and the corresponding solution is derived analytically by solving a group of non-homogeneous partial differential equations. The proposed solution is in good agreement with the finite element solution and exhibits higher accuracy compared to the Euler–Bernoulli beam solution that relies on the assumption of transverse shear deformation and isotropy. An extensive investigation is carried out to analyze how the bending behavior of TCC beams is influenced by variations in interfacial shear stiffness and temperature field.

Keywords: timber–concrete composite beam; thermo-mechanical condition; orthotropy; non-uniform temperature field; interface slip

Citation: Guan, B.; Dai, Y.; Zhang, T.; Wu, P.; Zhang, J. Theoretical Analysis on Thermo-Mechanical Bending Behavior of Timber–Concrete Composite Beams. *Buildings* **2023**, *13*, 3101. https://doi.org/10.3390/buildings13123101

Academic Editor: Rajai Zuheir Al-Rousan

Received: 21 November 2023
Revised: 10 December 2023
Accepted: 12 December 2023
Published: 14 December 2023

1. Introduction

As one sustainable bio-based building material, the increased use of 1% timber to replace building materials (i.e., steel, brick, concrete, etc.) in construction can reduce greenhouse gas emissions by about 1.2% accordingly. With advantages such as environmental friendliness, lightweight, sound insulation, ease of processing, and visual appeal, timber–concrete composite (TCC) beams have wide application in the field of construction engineering [1–3]. As a structural member, the TCC beam combines the advantages of both timber and concrete. There are two key points for the design and application of TCC beams. The first is that the biological and morphological characteristics of timber, including cell direction, cell wall feature, and growth ring, lead to significantly different properties along the longitudinal, radial, and tangential directions [4]. The other is that the interfacial slip between timber and concrete occurs more or less because of the limited stiffness shear connector [5]. In addition, the TCC beam is often subjected to both a mechanical load and a temperature environment; meanwhile, the properties of heat conductivity and thermal expansion are different between timber and concrete. Such a problem is important for the design and application of TCC beams, and it deserves to be investigated in depth.

For the mechanical behaviors of TCC under thermo-mechanical conditions, several studies have been reported. Fonseca et al. [6] introduced a numerical model to forecast the impact of wood density on unshielded wood connections featuring an internal steel plate, relative to those connections employing passive protection via gypsum plasterboard, under fire exposure. By using ANSYS software version 2022R1, Carlos Gomes et al. [7] performed thermodynamic numerical analysis on the connection between steel and wood. They verified how wood density affects the transmission of heat via connections during fires and introduced a thermodynamic composite model designed to address and analyze these

specific issues. By conducting one environmental temperature short-term destructive test and five full-scale fire tests on glulam–concrete composite beams, Du et al. [8] extensively investigated the effects of the load ratio, presence of timber boards, and fire-resistant gypsum boards on temperature distribution and fire resistance performance. Meena et al. [9] provided an examination, both via experimentation and numerical analysis, of the heat resistance properties of an innovative TCC setup with timber beams at the top and a concrete layer at the bottom. Lange et al. [10] explored the effects of non-standard fires on timber components and extended the simplified cross-section method used for structural calculations to parametric fire exposures. Le et al. [11] conducted a practical assessment of the fire resistance of timber–steel composites and expanded the knowledge associated with this composite material during the destructive process. Liu et al. [12] conducted a research study which presents temperature resistance test results of three large-scale TCC floor specimens and the development of a finite element modeling methodology for TCC floors under temperature-mechanical coupling effects. Zhang and Wang [13] proposed an energy-based time equivalent method and validated its effectiveness via experiments. This method can be used to evaluate the fire resistance of TCC structures under the improved travelling fires methodology's fire conditions. The one-way coupling method, utilizing computational fluid dynamics and the finite element method, was employed by Matías et al. [14] to study the thermo-mechanical response of steel–wood structures during a heated environment. The use of on-site applied fire-retardant treatments was investigated by Laranjeira et al. [15] to protect the existing timber roof structures from the impact of fire. Qin et al. [16] conducted experiments to assess the fire behavior of wooden components under various loads and proposed the impact mechanisms of load conditions on the fire behavior of wood. Shi et al. [17] employed a three-dimensional nonlinear finite element model to investigate the influence of various factors, including heating time, groove length, groove beam width, groove depth, screw diameter, and screw penetration length, on the shear behavior of grooved connectors in glulam–concrete composite beams subjected to temperature conditions. Taking into account that the TCC concrete layer experiences compressive forces during bending while the timber beams are subjected to tensile forces, Hehl et al. [18] have conducted a study that incorporates thermal and fire protection functionality into the connection system of a novel TCC setup, where timber beams are positioned on the upper side and a concrete layer is located beneath. Djoubissie et al. [19] conducted an experimental study on the mechanical behavior of timber–concrete shear connections using threaded reinforcing bars and presented the experimental results of push-out tests on simple timber–concrete connection systems. Focusing on current industry practices, Siddika et al. [20] conducted a review of the existing guidelines for CLT-concrete floor systems and provided details on the fundamental requirements regarding system design, construction, and performance. Mirdad et al. [21] developed an analytical model that takes into account the behavior of interlayer connectors under the elastic-plastic range, as well as the acoustic layer between timber and concrete, to accurately predict the load-carrying capacity and failure modes of mass timber panel–concrete composite floor systems. Based on the "γ-method", Shi et al. [22] summarized the experimental schemes and theoretical analysis of the flexural behavior of prestressed and non-prestressed TCC beams. Zhang et al. [23] established an empirical formula for determining the shear stiffness of notched connections based on numerical simulations. They compared the predicted flexural stiffness of the composite beam model, with discrete bonding, with the experimental results to validate the accuracy of the proposed formula. Sebastian et al. [24] quantified the effective flexural stiffness to capture the material nonlinearity induced by the bending-slip effect in TCC sections. They utilized a B profile that satisfies equilibrium and compatibility and is linked to the nonlinear constitutive behavior of the connection for analysis.

In the aforementioned literature, the mechanical behavior of laminated beams in a thermal environment was primarily investigated using experimental, numerical simulation, and analytical approaches. The experimental method is widely regarded as the most reli-

able means of conducting scientific research. However, it is time consuming and expensive, particularly when conducting parameter studies involving multiple conditions. On the other hand, numerical simulation, which relies on computing hardware and programming, offers flexibility, applicability, and cost effectiveness compared to the experimental methods. It is commonly employed to address complex scientific and engineering problems. Additionally, the analytical method, which is based on precise theories, is also crucial. It serves as a benchmark to validate other simplified solutions and has inherent advantages in revealing the physical mechanisms of the problem.

Various theories exist for the analysis of composite beams. The Euler–Bernoulli beam theory, a classical approach to bending, is widely recognized as a fundamental method. This theory, however, overlooks the impact of transverse shear deformation on bending solutions [25]. Timoshenko pioneered the study of thick beams by considering transverse shear deformation and assuming a constant transverse shear strain along the beam thickness [26]. In pursuit of enhanced accuracy in predicting transverse shear deformation, higher-order theories have been introduced. These advanced theories aim to account for the complexities associated with transverse shear deformation [27–29].

This paper presents an analytical solution based on the thermo-elasticity theory to investigate the thermo-mechanical bending behavior of TCC beams with considered interfacial shear stiffness. Since the thermo-elasticity theory involves no assumption of transverse shear deformation, it surpasses the accuracy of simplified theories such as the Euler–Bernoulli beam theory, Timoshenko beam theory, and higher-order shear deformation theories. In the analytical process, the non-uniform temperature field is solved based on the two-dimensional heat conduction theory by means of Fourier series expansion. Then, the analytical solution of stresses and displacements is derived out by solving a group of non-homogeneous partial differential equations. The proposed solution obtained is compared with existing solutions. Furthermore, a comprehensive parameter study is conducted on the impact of interfacial shear stiffness and temperature gradient on the bending behavior of TCC beams. The analysis results serve as a valuable reference for understanding the response of laminated beams to thermal-mechanical loads in practical engineering applications.

2. Analytical Model

A TCC beam with length L and height H, composed of concrete flange and timber web bonded via discontinuous steel shear connectors, is taken as the research object as shown in Figure 1. The shear stiffness of any shear connector is k_0 and the adjacent spacing is l_0. To predict the overall mechanical performance, the discontinuous shear connectors are equivalent to a continuous interface with interfacial shear stiffness k_s, in which $k_s = k_0/l_0$. The TCC beam is simply supported at two edges, subjected to a mechanical load $q(x)$ on the top surface and exposed to non-uniform thermal shock with T^t and T^b respectively applied on the top and bottom surfaces, in which T means the relative temperature with respect to the reference temperature T_0. The width and the height of each constituent part are b_i and h_i, respectively. The part index is denoted by i, and i = 1 or 2, which means the concrete or timber. The elastic modulus, shear modulus, Poisson's ratio, heat conductivity coefficient, and thermal expansion coefficient are denoted by E, G, μ, λ and α, respectively.

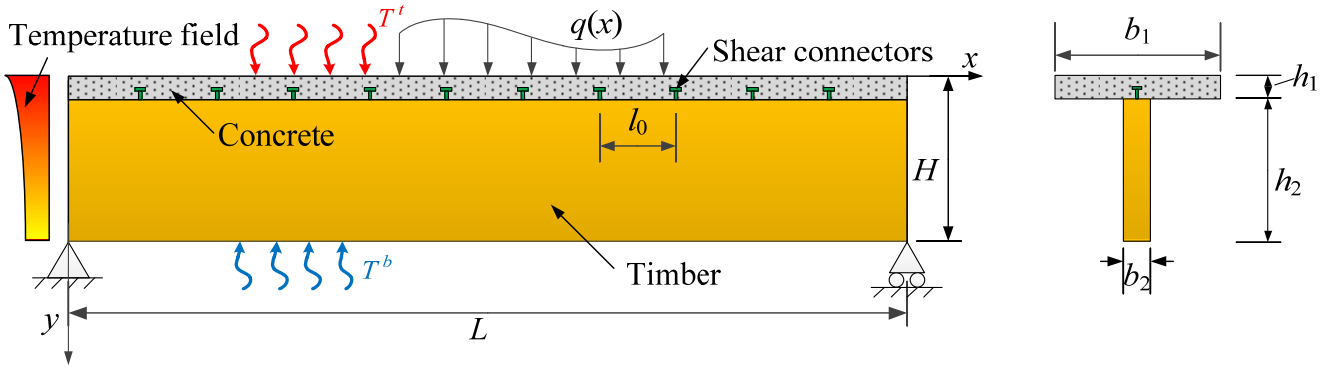

Figure 1. TCC beam under thermo-mechanical condition.

2.1. Assumptions and Applicable Conditions

The assumptions and applicable conditions of the proposed analytical model for the TCC beam include:

(1) The mechanical property of the TCC beam is within the linear elastic range;
(2) The absolute temperature considered is less than 100 °C and only the thermal deformation and stress are taken into account, while the ultra-high temperature, which leads to fire or material property change, is out of the scope of the present study;
(3) The shear lag effect of the concrete flange is neglected.

2.2. Temperature Field

In order to study the stresses and displacements of the TCC beam under a thermo-mechanical load, its temperature field is determined in this section. In the present study, the temperature field is considered in steady state. Based on the two-dimensional heat conduction theory [30], the temperature field and the heat flux for the i^{th} (i = 1,2) component should satisfy the following equations

$$(\frac{\partial^2}{\partial x^2} + \frac{\partial^2}{\partial y^2})T^i = 0,\ F^i = -\lambda_i \frac{\partial T^i}{\partial y}, \tag{1}$$

where T^i and F^i denote the temperature field and the heat flux of the i^{th} component, respectively. Such kind of partial differential equation can be solved via the separating variable method. By separating the variable and then expanding the temperature field into a Fourier series in the x direction, one obtains

$$T^i = \sum_{m=1}^{\infty} T_m^i(y)\sin(\beta_m x), \tag{2}$$

where $\beta_m = m\pi x/L$.

By substituting Equation (2) into (1), the general solutions for T^i and F^i are obtained as

$$\begin{aligned} T^i &= \sum_{m=1}^{\infty} [\cosh(\beta_m y)A_1^{im} + \sinh(\beta_m y)A_2^{im}]\sin(\beta_m x), \\ F^i &= \sum_{m=1}^{\infty} [-\lambda_i\beta_m \sinh(\beta_m y)A_1^{im} - \lambda_i\beta_m \cosh(\beta_m y)A_2^{im}]\sin(\beta_m x), \end{aligned} \tag{3}$$

where A_1^{im} and A_2^{im} are undermined yet. Meanwhile, T^i and F^i are continuous at the interface between adjacent components, i.e.,

$$T^i(d_i) = T^{i+1}(d_i),\ b_i F^i(d_i) = b_{i+1}F^{i+1}(d_i), \tag{4}$$

where $d_i = \sum_{j=1}^{i} h_j$. The given temperature conditions on the beam surfaces are also expanded into a Fourier series

$$T^1(x,0) = T^t = \sum_{m=1}^{\infty} [2T^t(1-\cos m\pi)/m\pi]\sin(\beta_m x),$$

$$T^4(x,H) = T^b = \sum_{m=1}^{\infty} [2T^b(1-\cos m\pi)/m\pi]\sin(\beta_m x). \quad (5)$$

There are four undetermined coefficients for each series item and four conditions, including three interfacial conditions and one surficial condition; thus, A_1^{im} and A_2^{im} for each component of the TCC beam can be solved uniquely. Substituting the results of A_1^{im} and A_2^{im} into Equation (3), the temperature field for each component in the TCC beam is obtained.

It should be pointed out that the proposed analytical model can also be extended to other imposed temperature conditions; for example, the convection and radiation [31]. For such a transient problem, the governing equations of temperature are related with the time variable, which can be tackled by using the technique of the separation of variables in conjunction with the linearized approximation [32].

2.3. Stresses and Displacements under Thermo-Mechanical Load

After the temperature field is determined, the stresses and displacements in the TCC beam under a thermo-mechanical load is then figured out in this section. On the basis of the two-dimensional thermo-elasticity theory in the linear elastic framework [30], the constitutive equation and the equilibrium equation for the i^{th} (i = 1,2) component are respectively given by

$$\frac{\partial u^i}{\partial x} = s_{11}^i\sigma_x^i + s_{12}^i\sigma_y^i + \alpha_i T^i,\ \frac{\partial v^i}{\partial y} = s_{12}^i\sigma_x^i + s_{22}^i\sigma_y^i + \alpha_i T^i,\ \frac{\partial u^i}{\partial y} + \frac{\partial v^i}{\partial x} = s_{66}^i\tau_{xy}^i, \quad (6)$$

$$\frac{\partial \sigma_x^i}{\partial x} + \frac{\partial \tau_{xy}^i}{\partial y} = 0,\ \frac{\partial \sigma_y^i}{\partial y} + \frac{\partial \tau_{xy}^i}{\partial x} = 0, \quad (7)$$

where σ, τ, u and v denote normal stress, shear stress, and x- and y-direction displacements, respectively, and

$$s_{11}^i = \frac{1}{E_x^i},\ s_{12}^i = -\frac{\mu_{xy}^i}{E_x^i} = -\frac{\mu_{yx}^i}{E_y^i},\ s_{22}^i = \frac{1}{E_y^i},\ s_{66}^i = \frac{1}{G_{xy}^i}.$$

The simply supported boundary condition can be expressed by

$$\sigma_x^i = v^i = 0, \text{ at } x = 0,\ L. \quad (8)$$

The stresses and displacements in the simply supported beam are expanded via a Fourier series, as follows

$$\begin{bmatrix} v^i \\ \sigma_x^i \\ \sigma_y^i \end{bmatrix} = \sum_{m=1}^{\infty} \begin{bmatrix} v_m^i(y) \\ \sigma_{x,m}^i(y) \\ \sigma_{y,m}^i(y) \end{bmatrix} \sin(\beta_m x),\ \begin{bmatrix} u^i \\ \tau_{xy}^i \end{bmatrix} = \sum_{m=1}^{\infty} \begin{bmatrix} u_m^i(y) \\ \tau_{xy,m}^i(y) \end{bmatrix} \cos(\beta_m x). \quad (9)$$

By utilizing the expanded expressions and substituting Equation (6) into (7), two non-homogeneous partial differential equations for the displacements are deduced as

$$\frac{-s_{22}^i{\beta_m}^2}{(s_{12}^i)^2 - s_{11}^i s_{22}^i} u_m^i(y) - \left[\frac{s_{12}^i}{(s_{12}^i)^2 - s_{11}^i s_{22}^i} + \frac{1}{s_{66}^i}\right]\beta_m \frac{\partial v_m^i(y)}{\partial y} - \frac{1}{s_{66}^i}\frac{\partial^2 u_m^i(y)}{\partial y^2} = \frac{(s_{22}^i - s_{12}^i)\beta_m}{(s_{12}^i)^2 - s_{11}^i s_{22}^i}\alpha_i T_m^i,$$

$$\frac{\beta_m^2}{s_{66}^i}v_m^i(y)+\left[\frac{s_{12}^i}{(s_{12}^i)^2-s_{11}^i s_{22}^i}+\frac{1}{s_{66}^i}\right]\beta_m\frac{\partial u_m^i(y)}{\partial y}+\frac{s_{11}^i}{(s_{12}^i)^2-s_{11}^i s_{22}^i}\frac{\partial^2 v_m^i(y)}{\partial y^2}=\frac{s_{11}^i-s_{12}^i}{(s_{12}^i)^2-s_{11}^i s_{22}^i}\alpha_i\frac{\partial T_m^i}{\partial y}. \quad (10)$$

The solution for the displacements are determined as

$$u^i=\sum_{m=1}^{\infty}\left[\left(\sum_{k=1}^{4}D_{1,k}^{im}(y)B_k^{im}\right)-\frac{\alpha_i}{\beta_m}\cosh(\beta_m y)A_1^{im}-\frac{\alpha_i}{\beta_m}\sinh(\beta_m y)A_2^{im}\right]\cos(\beta_m x),$$

$$v^i=\sum_{m=1}^{\infty}\left[\left(\sum_{k=1}^{4}D_{2,k}^{im}(y)B_k^{im}\right)+\frac{\alpha_i}{\beta_m}\sinh(\beta_m y)A_1^{im}+\frac{\alpha_i}{\beta_m}\cosh(\beta_m y)A_2^{im}\right]\sin(\beta_m x), \quad (11)$$

where the detail of $D_{*,k}^{im}(y)$ is given in Appendix A, and the coefficient B_k^{im} is unknown yet. Substituting Equation (11) into (7) yields the solution for the stresses

$$\sigma_x^i=\sum_{m=1}^{\infty}\sum_{k=1}^{4}S_{1,k}^{im}(y)B_k^{im}\sin(\beta_m x),\ \sigma_y^i=\sum_{m=1}^{\infty}\sum_{k=1}^{4}S_{2,k}^{im}(y)B_k^{im}\sin(\beta_m x),\tau_{xy}^i=\sum_{m=1}^{\infty}\sum_{k=1}^{4}S_{3,k}^{im}(y)B_k^{im}\cos(\beta_m x), \quad (12)$$

where the detail of $S_{*,k}^{im}(y)$ is given in Appendix A.

At the interface, the forces at both sides of the interface, equal to the product of the corresponding stresses and the width, satisfy the equilibrium condition. In addition, the interfacial slip occurs because the shear connector can only provide finite stiffness. The present study only considers the mechanical behavior in the linear elastic range, and the interfacial slip and interfacial shear force are considered to meet Hooke's law. Hence, the stresses and displacements at the interface between adjacent components have the following relationship:

$$b_1\sigma_y^1(x,d_1)-b_2\sigma_y^2(x,d_1)=0,\ b_1\tau_{xy}^1(x,d_1)-b_2\tau_{xy}^2(x,d_1)=0,$$

$$[u^2(x,d_i)-u^1(x,d_i)]/k_s=b_1\tau_{xy}^1(x,d_1),\ v^1(x,d_1)-v^2(x,d_1)=0. \quad (13)$$

The stress condition at the top and the bottom of the beam is known as

$$\sigma_y^1(x,d_0)=q(x)=\frac{2}{L}\left[\int_0^L q(x)\sin(\beta_m x)dx\right]\sin(\beta_m x),$$

$$\tau_{xy}^1(x,d_0)=\sigma_y^2(x,d_2)=\tau_{xy}^2(x,d_2)=0. \quad (14)$$

Since A_1^{im} and A_2^{im} are determined in Section 2.1, there are eight undetermined coefficients for each series item, i.e., B_k^{im} and eight conditions, including six interfacial conditions and two surficial conditions, and thus, B_k^{im} for each component of the TCC beam can be solved uniquely. In the end, the solution of stresses and displacements at any position in the TCC beam under a thermo-mechanical load is obtained.

Although the proposed analytical model only gives a solution for a two-layer TCC beam, it can also be extended to a multilayered case, such as glued laminated timber beams, steel–concrete composite I-beams, etc. For this case, the present method to solve the undetermined coefficients can be replaced by the transfer matrix method [33,34], an efficient tool for multilayered composites.

3. Results and Discussion

In this section, the proposed solution is compared against the existing results, and the bending behavior of simply-supported TCC beam in the thermo-mechanical condition is analyzed through varying parameters. The default values of geometric and material parameters are L = 8000 mm, b_1 = 400 mm, h_1 = 80 mm, b_2 = 120 mm, h_2 = 300 mm, E^1 = 34.5 GPa,

$\mu^1 = 0.2$, $\lambda^1 = 1.28$ W/(mK), $\alpha^1 = 1.1 \times 10^{-5}/°C$, $E_x^2 = 14.2$ GPa, $E_y^2 = 1.12$ GPa, $G_{xy}^2 = 0.895$ GPa, $\mu^2 = 0.325$, $\lambda^2 = 0.15$ W/(mK), and $\alpha^2 = 2 \times 10^{-5}/°C$ [35,36], unless otherwise stated. The top surface of the TCC beam is subjected to mechanical load $q(x) = 0.01$ N/mm^2 and relative temperature $T^t = 30$ °C, $T^b = 0$ °C, with reference temperature $T_0 = 20$ °C. The default parameters are taken as above, unless otherwise specified.

3.1. Comparison Analysis

The proposed solution is validated by comparing it with both the finite element (FE) solution obtained using ABAQUS software version 2022 and the analytical solution based on the Euler–Bernoulli (EB) beam theory [37] for orthotropic materials. Since the EB solution only gives the results under a mechanical load, for the sake of comparison, the TCC beam considered here is subjected to a mechanical load. The geometric and material parameters are taken as default values and $k_s = 10^5$ MPa, while L is variable. The FE model shown in Figure 2, the concrete and timber, are modeled via the C3D8R element, with 9200 elements used in total. The interfacial distributed shear connectors is described by a Hookean spring and modeled via the Spring-2 element, in which each Spring-2 element connects the adjacent mesh nodes of timber and concrete. Since the TCC beam is studied in the linear elastic range, the contact friction problem of shear connectors is not considered. The contact friction problem is obvious for nonlinear behavior of the TCC beam, e.g., the case that the shear connector pulls out of the timber or concrete, and in this case, the interface can be modeled using the surface-to-surface contact [38]. The simply-supported boundary condition for the TCC beam is set the same as Equation (8), i.e., the y-direction degree of freedom is restrained at the two edges of the TCC beam, and in addition, the x-direction and z-direction degrees of freedoms are restrained at the origin point ($x = 0$, $y = 0$) to avoid the rigid body displacement. For this linear elastic problem, the type of analysis is set as a static general case. Table 1 presents the results of σ_x ($L/2$, 0), τ_{xy} (0, $h_1 + 0.5h_2$) and v ($L/2$, H) from the proposed FE and EB solutions across different L/H ratios. Observations reveal that the current solution aligns closely with the FE solution, exhibiting errors consistently below 3% for all cases. The error is mainly caused by reason that the shear lag effect is neglected in the proposed analytical solution. Furthermore, the current solution corresponds to the EB solution for slender beams, but discrepancies increase as L/H decreases. The errors of σ_x, τ_{xy} and v reach 10.6%, 21.6%, and 48.3%, respectively, as $L/H = 5$. These errors predominantly stem from neglecting transverse shear deformation and the orthotropy in the EB theory.

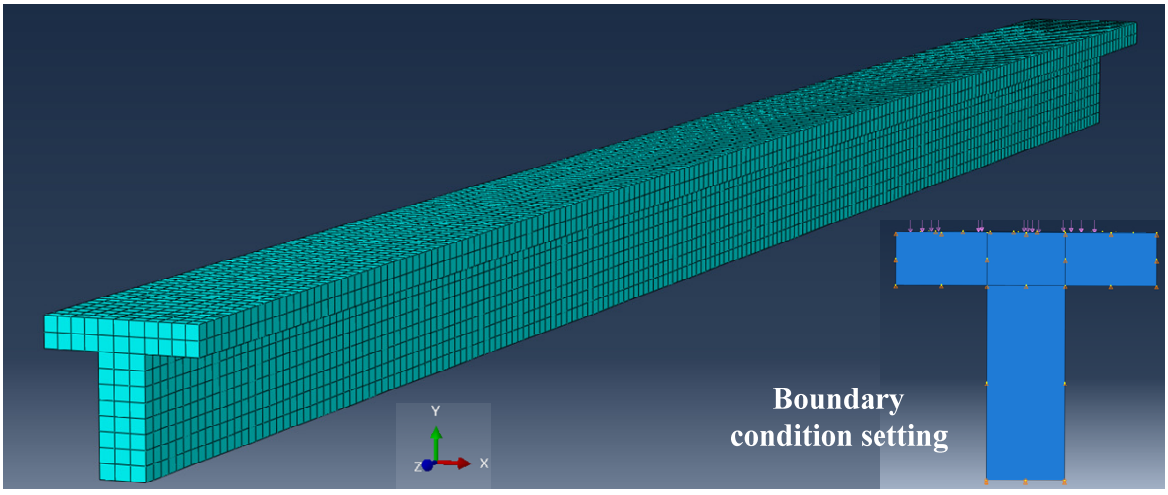

Figure 2. FE model and boundary condition setting.

Table 1. Results of σ_x $(L/2, 0)$, τ_{xy} $(0, h_1 + 0.5h_2)$ and v $(L/2, H)$ from the proposed FE and EB solutions with different L/H ratios.

L/H	Solution	Proposed	FE	EB	Error of FE	Error of EB
20	σ_x [MPa]	13.56	13.80	13.27	1.77%	2.14%
	τ_{xy} [MPa]	−0.7418	−0.7564	−0.7720	1.97%	4.07%
	v [mm]	−21.94	−22.46	−22.41	2.38%	2.14%
15	σ_x [MPa]	7.669	7.781	7.465	1.46%	2.66%
	τ_{xy} [MPa]	−0.5478	−0.5599	−0.5790	2.20%	5.70%
	v [mm]	−7.316	−7.390	−7.092	1.01%	3.06%
10	σ_x [MPa]	3.459	3.499	3.318	1.16%	4.08%
	τ_{xy} [MPa]	−0.3533	−0.3631	−0.3860	2.78%	9.26%
	v [mm]	−1.654	−1.680	−1.401	1.57%	15.3%
5	σ_x [MPa]	0.928	0.9506	0.8294	2.44%	10.6%
	τ_{xy} [MPa]	−0.1587	−0.1623	−0.1930	2.26%	21.6%
	v [mm]	−0.1692	−0.1730	−0.08756	2.24%	48.3%

3.2. Parameter Analysis

Figure 3 demonstrates the variations in the stresses and displacements of the TCC beam with respect to k_s under pure mechanical (PM), pure thermal (PT), and thermo-mechanical (MT) conditions, respectively. From Figure 3, it is evident that under the PM condition, and when $10 < k_s < 10^5$ MPa, there is a sharp decline for σ_x, u, τ_{xy} and v, whereas the stresses and displacements remain constant in the rest ranges. For the ranges of $k_s < 10$ MPa and $k_s > 10^5$ MPa, it can be referred to as no connection and perfect connection. Conversely, under PT condition, when $10 < k_s < 10^5$ MPa, the variations in the stresses and displacements are opposite to those observed under the PM condition. As k_s increases, the corresponding manufacturing cost also increases, and Figure 3a–d indicates that the optimum cost effectiveness is achieved when the k_s is around 10^5 MPa. At the interface, τ_{xy} tends to zero when $10^{-2} < k_s < 10$ MPa. And, with the increasing k_s, the absolute value of τ_{xy} under the PM and PT conditions both increase, but the stress directions are opposite. Under the combined action of the PM and PT conditions, the behavior of σ_x, u, τ_{xy} and v is consistent with the results of the mechanical-thermal coupling, adhering to the superposition principle.

Figure 4 shows the y-direction distribution of stresses and displacements of the TCC beam under the PM and PT conditions with different shear stiffnesses, respectively. From Figure 4, it is found that the y-direction distributions of σ_x and u exhibit a zigzag pattern. The slope of σ_x with respect to y in the concrete is larger than that in the timber because of the difference of modulus, while the slopes of u are the same in the concrete and timber. τ_{xy} shows a multi-peaked pattern and has large jump at the interface, while v is almost unchanged in the y direction. In addition, the directions and change laws of stresses are roughly the same in the concrete and the timber parts for the PM condition but totally opposite for the PT condition. This is because for the PM condition, the concrete and the timber parts resist the external mechanical load together, and as the combination effect, i.e., the interfacial shear stiffness k_s, increases, the stresses decrease. On the contrary, for the PT condition, the concrete and the timber parts resist each other because of the difference in thermal deformation. As the interfacial shear stiffness k_s increases, the resistance effect becomes obvious and this leads to the stresses in the PT condition enlarging. The different mechanisms of the TCC beam from the PM and PT conditions are important for practical engineering. For a good design of the TCC beam under the thermo-mechanical condition, the stresses and displacements respectively from the PM and PT conditions can be partly offset in order to reduce the overall deflection or maximum stress.

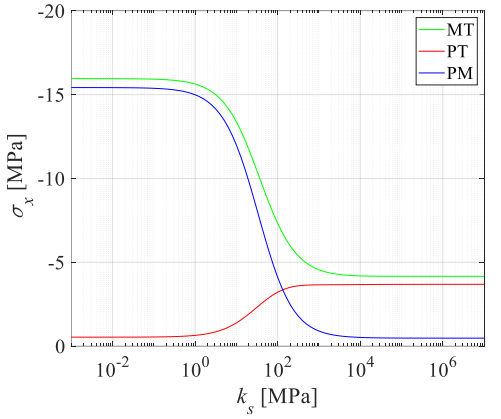

(**a**) σ_x ($L/2$, h_1)

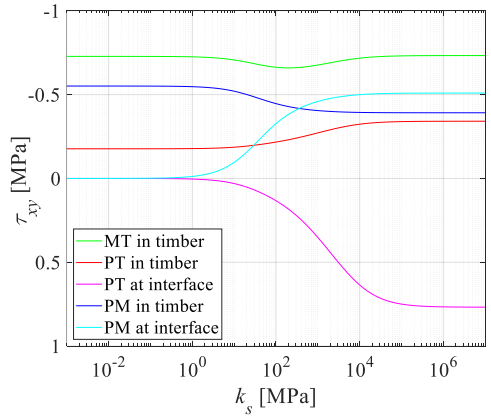

(**b**) τ_{xy} (0, $h_1 + 0.5h_2$)

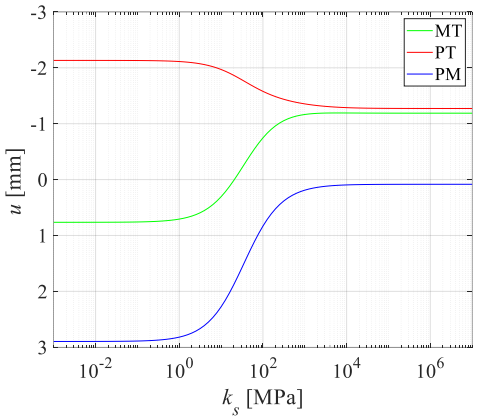

(**c**) u (0, 0)

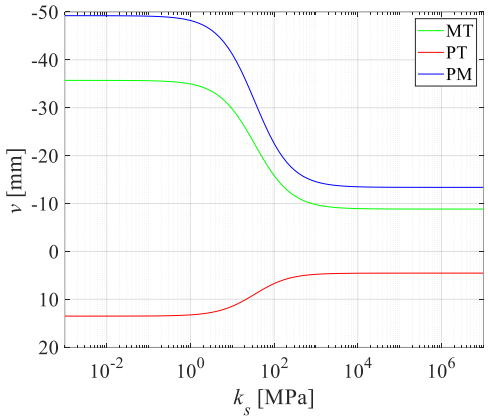

(**d**) v ($L/2$, 0)

Figure 3. Variations in stresses and displacements of TCC beam with respect to interfacial stiffness under PM, PT, and MT conditions, respectively.

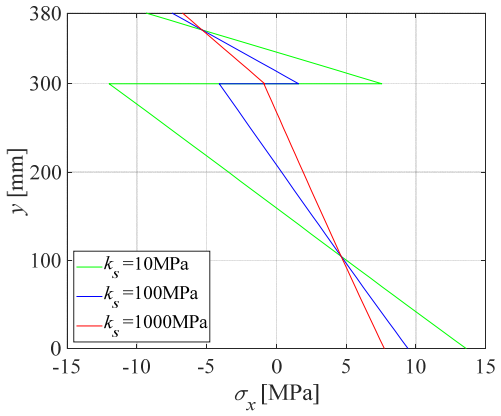

(**a**) σ_x at $x = L/2$ in PM

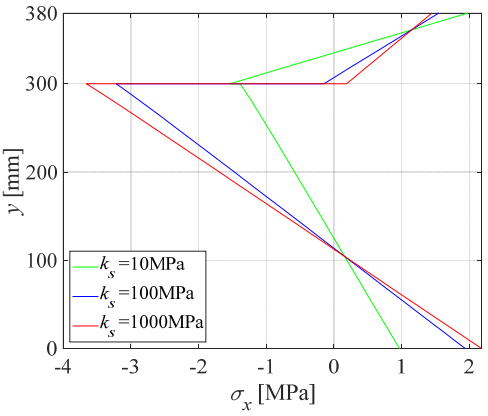

(**b**) σ_x at $x = L/2$ in PT

Figure 4. *Cont.*

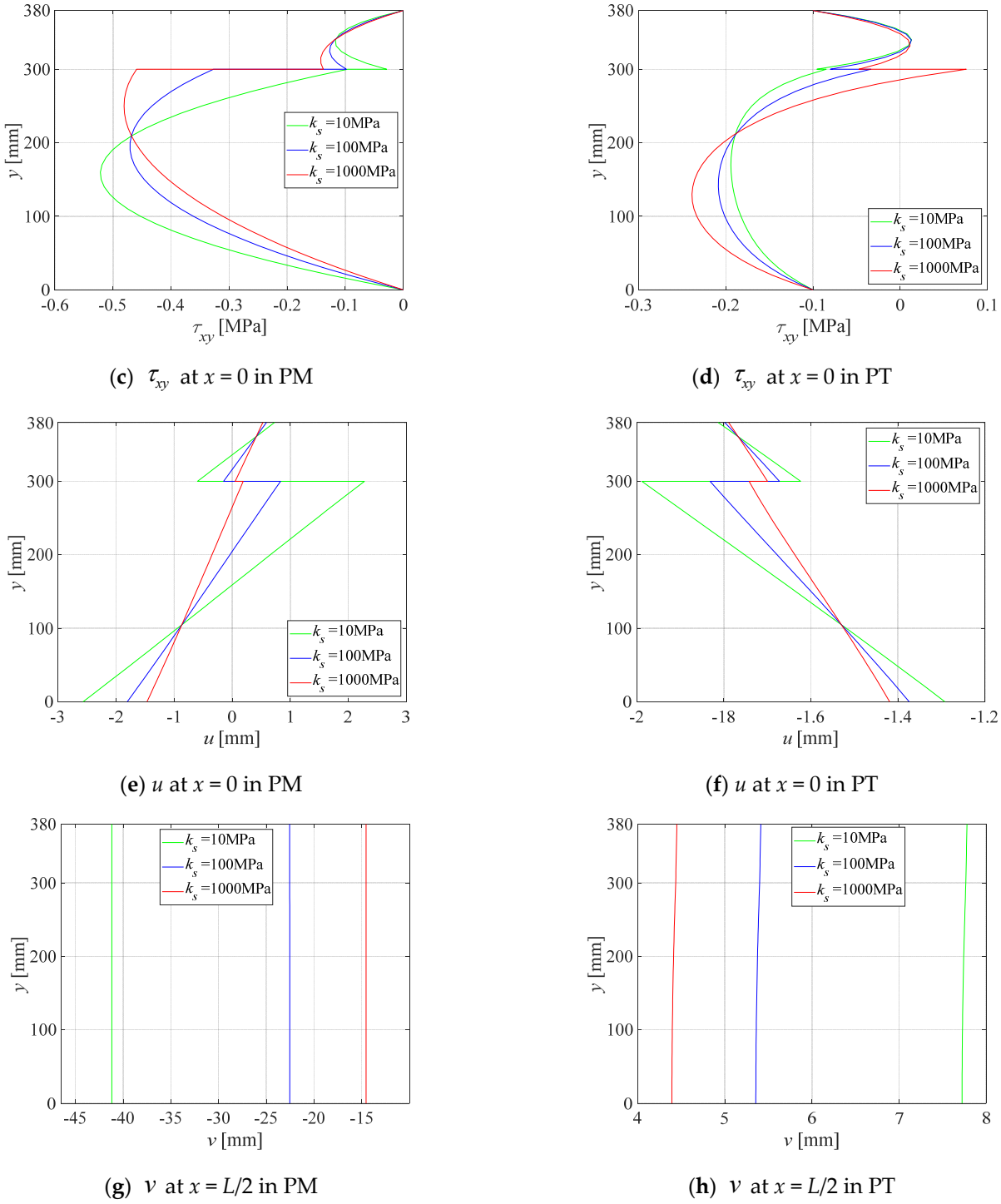

(**c**) τ_{xy} at $x = 0$ in PM

(**d**) τ_{xy} at $x = 0$ in PT

(**e**) u at $x = 0$ in PM

(**f**) u at $x = 0$ in PT

(**g**) v at $x = L/2$ in PM

(**h**) v at $x = L/2$ in PT

Figure 4. Distribution of stresses and displacements of TCC beam under PM and PT conditions with different interfacial stiffness, respectively.

Figure 5 shows the y-direction distribution of stresses and displacements of the TCC beam under the PT condition with k_s = 1000 MPa for different surficial temperature difference, i.e., T^b = 0 °C, T^t = 10, 30, 50 °C, respectively. It can be found that σ_x, u, τ_{xy} and v all increase with rising the surficial temperature difference, primarily due to the difference of thermal expansion between the concrete and timber parts. The maximum values of σ_x and τ_{xy} occur at the interface between timber and concrete, attributable to the differences in the characteristics of the two materials. As T^t increases, the temperature field in concrete

increases more significantly than that in timber. Thus, u in concrete is larger than that in timber, but the stresses in concrete are less than those in timber.

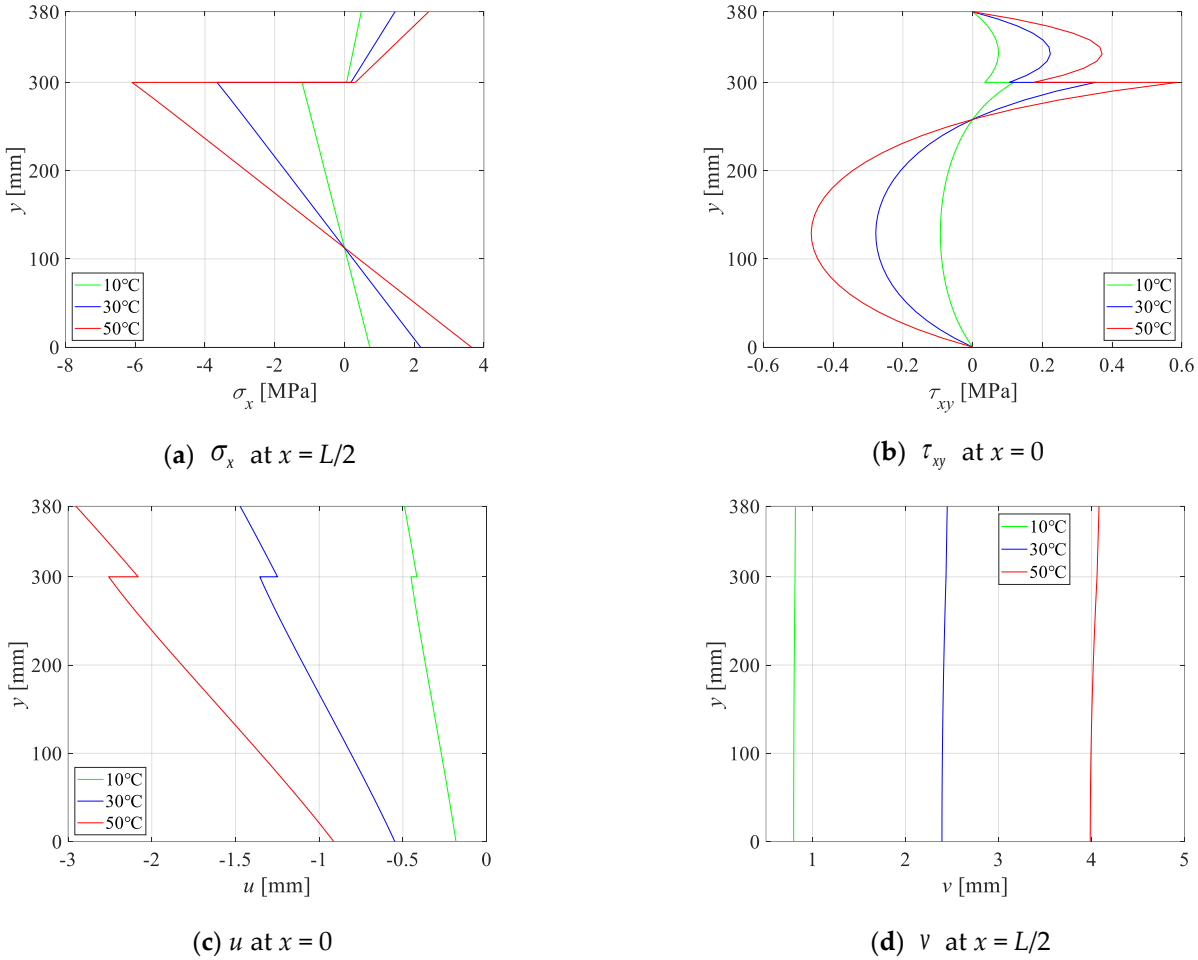

(**a**) σ_x at $x = L/2$ (**b**) τ_{xy} at $x = 0$

(**c**) u at $x = 0$ (**d**) v at $x = L/2$

Figure 5. Distribution of stresses and displacements of TCC beam under PT condition with different surficial temperature difference, i.e., T^b = 0 °C, T^t = 10, 30, 50 °C, respectively.

4. Conclusions

Focusing on the bending of the TCC beam subjected to a mechanical load and a non-uniform temperature field, an analytical solution is presented. This solution, rooted in thermo-elasticity theory, considers the anisotropy of timber, shear deformation, as well as interfacial slip. The primary conclusions derived from this study are summarized as follows:

1. The proposed solution is in good agreement with the finite element result and offers higher accuracy compared to the simplified Euler–Bernoulli theory-based solution, which neglects the transverse shear deformation and the orthotropy of the TCC beam.
2. The stresses and displacements vary with interfacial shear stiffness only in a certain range and remain constant in the rest ranges, which are actually no connection and perfect connection limits. The variations in the stresses and displacements under the pure thermal condition are opposite to those observed under pure mechanical loading. At the interface, with the increasing interfacial shear stiffness, the shear stress under pure mechanical and pure thermal conditions both increase, but the stress directions are opposite. The superposition principle is suitable for the stresses and displacements of the TCC beam under the thermo-mechanical condition.
3. The stresses decrease with interfacial shear stiffness for the pure mechanical condition but have the opposite change law for the pure thermal condition. On the contrary,

the displacements have the same change law. This is because for the TCC beam in the PM condition, the concrete and the timber parts resist the external mechanical load together, and as the combination effect increases, the stresses decrease. On the contrary, for the PT condition, the concrete and the timber parts resist each other because of the difference in thermal deformation. As the interfacial shear stiffness increases, the resistance effect becomes obvious and this leads to the stresses in the PT condition enlarging. The different mechanisms of the TCC beam from the PM and PT conditions are important for practical engineering. For a good design of the TCC beam under the thermo-mechanical condition, the stresses and displacements respectively from the PM and PT conditions can be partly offset in order to reduce the overall deflection or maximum stress.

4. The stress and displacement levels elevate as the surface temperature difference increases, mainly because of the distinct thermal expansion rates between concrete and timber. Additionally, the highest stress values manifest at the timber–concrete interface due to disparities in the material characteristics.

As a future work, the proposed analytical model will be extended to consider the coupling thermo-mechanical behavior of timber–concrete composite beams under high temperature, which leads to temperature-dependent material property. In addition, this can also be extended to the multilayered case, such as glued laminated timber beams, steel–concrete composite I-beams, etc., via the transfer matrix method.

Author Contributions: Methodology, P.W.; Software, Y.D.; Validation, T.Z.; Investigation, B.G.; Writing—original draft, B.G.; Writing—review & editing, P.W.; Supervision, J.Z.; Project administration, J.Z. All authors have read and agreed to the published version of the manuscript.

Funding: This work was supported by the National Natural Science Foundation of China (Grant No. 52108220).

Data Availability Statement: The data presented in this study are available on request from the corresponding author. The data are not publicly available due to commercial restrictions.

Conflicts of Interest: The authors declare that they have no known competing financial interests or personal relationships that could have appeared to influence the work reported in this paper.

Appendix A

The details of $D^{im}_{*,k}(y)$ and $S^{im}_{*,k}(y)$ in Equations (11) and (12) are given by

$$D^{im}_{1,1} = (s^i_{12}\beta_m - \frac{s^i_{11}}{\beta_m}\frac{f^1_{mi}-f^2_{mi}}{2s^i_{11}})e^{-y\sqrt{\frac{f^1_{mi}-f^2_{mi}}{2s^i_{11}}}},\ D^{im}_{1,2} = (s^i_{12}\beta_m - \frac{s^i_{11}}{\beta_m}\frac{f^1_{mi}-f^2_{mi}}{2s^i_{11}})e^{y\sqrt{\frac{f^1_{mi}-f^2_{mi}}{2s^i_{11}}}},$$

$$D^{im}_{1,3} = (s^i_{12}\beta_m - \frac{s^i_{11}}{\beta_m}\frac{f^1_{mi}+f^2_{mi}}{2s^i_{11}})e^{-y\sqrt{\frac{f^1_{mi}+f^2_{mi}}{2s^i_{11}}}},\ D^{im}_{1,4} = (s^i_{12}\beta_m - \frac{s^i_{11}}{\beta_m}\frac{f^1_{mi}+f^2_{mi}}{2s^i_{11}})e^{y\sqrt{\frac{f^1_{mi}+f^2_{mi}}{2s^i_{11}}}},$$

$$D^{im}_{2,1} = (s^i_{22}\beta^2_m\sqrt{\frac{2s^i_{11}}{f^1_{mi}-f^2_{mi}}} - s^i_{12}\sqrt{\frac{f^1_{mi}-f^2_{mi}}{2s^i_{11}}})e^{-y\sqrt{\frac{f^1_{mi}-f^2_{mi}}{2s^i_{11}}}},\ S^{im}_{1,1} = \frac{f^1_{mi}-f^2_{mi}}{2s^i_{11}}e^{-y\sqrt{\frac{f^1_{mi}-f^2_{mi}}{2s^i_{11}}}},$$

$$D^{im}_{2,2} = -(s^i_{22}\beta^2_m\sqrt{\frac{2s^i_{11}}{f^1_{mi}-f^2_{mi}}} - s^i_{12}\sqrt{\frac{f^1_{mi}-f^2_{mi}}{2s^i_{11}}})e^{y\sqrt{\frac{f^1_{mi}-f^2_{mi}}{2s^i_{11}}}},\ S^{im}_{1,2} = \frac{f^1_{mi}-f^2_{mi}}{2s^i_{11}}e^{y\sqrt{\frac{f^1_{mi}-f^2_{mi}}{2s^i_{11}}}},$$

$$D^{im}_{2,3} = (s^i_{22}\beta^2_m\sqrt{\frac{2s^i_{11}}{f^1_{mi}+f^2_{mi}}} - s^i_{12}\sqrt{\frac{f^1_{mi}+f^2_{mi}}{2s^i_{11}}})e^{-y\sqrt{\frac{f^1_{mi}+f^2_{mi}}{2s^i_{11}}}},\ S^{im}_{1,3} = \frac{f^1_{mi}+f^2_{mi}}{2s^i_{11}}e^{-y\sqrt{\frac{f^1_{mi}+f^2_{mi}}{2s^i_{11}}}},$$

$$D^{im}_{2,4} = -(s^i_{22}\beta^2_m\sqrt{\frac{2s^i_{11}}{f^1_{mi}+f^2_{mi}}} - s^i_{12}\sqrt{\frac{f^1_{mi}+f^2_{mi}}{2s^i_{11}}})e^{y\sqrt{\frac{f^1_{mi}+f^2_{mi}}{2s^i_{11}}}},\ S^{im}_{1,4} = \frac{f^1_{mi}+f^2_{mi}}{2s^i_{11}}e^{y\sqrt{\frac{f^1_{mi}+f^2_{mi}}{2s^i_{11}}}},$$

$$S^{im}_{2,1} = -\beta^2_m e^{-y\sqrt{\frac{f^1_{mi}-f^2_{mi}}{2s^i_{11}}}},\ S^{im}_{2,2} = -\beta^2_m e^{y\sqrt{\frac{f^1_{mi}-f^2_{mi}}{2s^i_{11}}}},\ S^{im}_{2,3} = -\beta^2_m e^{-y\sqrt{\frac{f^1_{mi}+f^2_{mi}}{2s^i_{11}}}}, S^{im}_{2,4} = -\beta^2_m e^{y\sqrt{\frac{f^1_{mi}+f^2_{mi}}{2s^i_{11}}}},$$

$$S^{im}_{3,1} = \beta_m\sqrt{\frac{f^1_{mi}-f^2_{mi}}{2s^i_{11}}}e^{-y\sqrt{\frac{f^1_{mi}-f^2_{mi}}{2s^i_{11}}}}, S^{im}_{3,2} = -\beta_m\sqrt{\frac{f^1_{mi}-f^2_{mi}}{2s^i_{11}}}e^{y\sqrt{\frac{f^1_{mi}-f^2_{mi}}{2s^i_{11}}}}, S^{im}_{3,3} = \beta_m\sqrt{\frac{f^1_{mi}+f^2_{mi}}{2s^i_{11}}}e^{-y\sqrt{\frac{f^1_{mi}+f^2_{mi}}{2s^i_{11}}}},$$

$$S^{im}_{3,4} = -\beta_m\sqrt{\frac{f^1_{mi}+f^2_{mi}}{2s^i_{11}}}e^{y\sqrt{\frac{f^1_{mi}+f^2_{mi}}{2s^i_{11}}}},$$

where

$$f^1_{mi} = 2\beta^2_m s^i_{12} + \beta^2_m s^i_{66},\ f^2_{mi} = \sqrt{4\beta^4_m(s^i_{12})^2 + 4\beta^4_m s^i_{12}s^i_{66} + \beta^4_m(s^i_{66})^2 - 4\beta^4_m s^i_{11}s^i_{22}}.$$

References

1. Ling, Z.; Li, Z.; Lu, F.; Yang, H.; Zheng, W.; Zhang, L. Flexural strengthening of timber-concrete composite beams using mechanically fastened and externally bonded combining mechanically fastened strengthening techniques. *J. Build. Eng.* **2023**, *78*, 107645. [CrossRef]
2. Tao, H.; Yang, H.; Zhang, J.; Ju, G.; Xu, J.; Shi, B. Nonlinear finite element analysis on timber-concrete composite beams. *J. Build. Eng.* **2022**, *51*, 104259. [CrossRef]
3. Shi, B.; Liu, W.; Yang, H. Experimental investigation on the long-term behavior of prefabricated timber-concrete composite beams with steel plate connections. *Constr. Build. Mater.* **2021**, *266*, 120892. [CrossRef] [PubMed]
4. Nero, R.; Christopher, P.; Ngo, T. Investigation of rolling shear properties of cross-laminated timber (CLT) and comparison of experimental approaches. *Constr. Build. Mater.* **2022**, *316*, 125897. [CrossRef]
5. Li, C.; Li, S.-C.; Yue, K.; Wu, P.; Xiao, Z.-P.; Zhang, J. Analytical solutions and optimization design for bending behavior of cross-laminated timber beams considering orthotropy and interface slip. *Case Stud. Constr. Mater.* **2023**, *18*, e01948. [CrossRef]
6. Piloto, P.A.G.; Fonseca, E.M.; Silva, L.; Leite, P.A. Numerical model to predict the effect of wood density in wood–steel–wood connections with and without passive protection under fire. *J. Fire Sci.* **2020**, *38*, 122–135.
7. Gomes, C.; Fonseca, E.M.M.; Lopes, H.M. Thermomechanical Analysis of Steel-to-Timber Connections under Fire and the Material Density Effect. *Appl. Sci.* **2022**, *12*, 10516. [CrossRef]
8. Du, H.; Hu, X.; Xie, Z.; Meng, Y. Experimental and analytical investigation on fire resistance of glulam-concrete composite beams. *J. Build. Eng.* **2021**, *44*, 103244. [CrossRef]
9. Meena, R.; Schollmayer, M.; Tannert, T. Experimental and Numerical Investigations of Fire Resistance of Novel Timber-Concrete-Composite Decks. *J. Perform. Constr. Facil.* **2014**, *28*, A4014009. [CrossRef]
10. Lange, D.; Boström, L.; Schmid, J.; Albrektsson, J. The Reduced Cross Section Method Applied to Glulam Timber Exposed to Non-standard Fire Curves. *Fire Technol.* **2015**, *51*, 1311–1340. [CrossRef]
11. Le, T.D.H.; Tsai, M.-T. Experimental Assessment of the Fire Resistance Mechanisms of Timber–Steel Composites. *Materials* **2019**, *12*, 4003. [CrossRef]
12. Liu, J.; Fischer, E.C.; Barbosa, A.R.; Sinha, A. Experimental Testing and Numerical Simulation of Timber-Concrete Composite Floors in Fire. *J. Struct. Eng.* **2023**, *149*, 04023151. [CrossRef]
13. Zhang, Y.; Wang, L. Energy-based time equivalent method for evaluating the fire resistance of timber–concrete composite structures exposed to travelling fires. *Struct. Infrastruct. Eng.* **2022**. [CrossRef]
14. Dellepiani, M.G.; Munoz, G.R.; Yanez, S.J.; Guzmán, C.F.; Flores, E.I.S.; Pina, J.C. Numerical study of the thermo-mechanical behavior of steel-timber structures exposed to fire. *J. Build. Eng.* **2023**, *65*, 105758. [CrossRef]
15. Laranjeira, J.P.D.; Cruz, H.; Pinto, A.P.F.; dos Santos, C.P.; Pereira, J.F. Reaction to Fire of Existing Timber Elements Protected with Fire Retardant Treatments: Experimental Assessment. *Int. J. Archit. Herit.* **2015**, *9*, 866–882. [CrossRef]

16. Qin, R.; Zhou, A.; Chow, C.L.; Lau, D. Structural performance and charring of loaded wood under fire. *Eng. Struct.* **2021**, *228*, 111491. [CrossRef]
17. Shi, D.; Hu, X.; Du, H.; Meng, Y.; Xie, Z. Thermo-mechanical analysis on shear behavior of grooved connectors for glulam-concrete composite beams under fire. *Fire Saf. J.* **2022**, *130*, 103594. [CrossRef]
18. Hehl, S.; Tannert, T.; Meena, R.; Vallee, T. Experimental and Numerical Investigations of Groove Connections for a Novel Timber-Concrete-Composite System. *J. Perform. Constr. Facil.* **2014**, *28*, A4014010. [CrossRef]
19. Djoubissie, D.D.; Messan, A.; Fournely, E.; Bouchaïr, A. Experimental study of the mechanical behavior of timber-concrete shear connections with threaded reinforcing bars. *Eng. Struct.* **2018**, *172*, 997–1010. [CrossRef]
20. Siddika, A.; Mamun, M.A.A.; Aslani, F.; Zhuge, Y.; Alyousef, R.; Hajimohammadi, A. Cross-laminated timber–concrete composite structural floor system: A state-of-the-art review. *Eng. Fail. Anal.* **2021**, *130*, 105766. [CrossRef]
21. Mirdad, M.A.H.; Chui, Y.H.; Tomlinson, D. Capacity and Failure-Mode Prediction of Mass Timber Panel–Concrete Composite Floor System with Mechanical Connectors. *J. Struct. Eng.* **2021**, *147*, 04020338. [CrossRef]
22. Shi, B.; Zhu, W.; Yang, H.; Liu, W.; Tao, H.; Ling, Z. Experimental and theoretical investigation of prefabricated timber-concrete composite beams with and without prestress. *Eng. Struct.* **2020**, *204*, 109901. [CrossRef]
23. Zhang, L.; Zhou, J.; Zhang, S.; Chui, Y.H. Bending stiffness prediction to mass timber panel-concrete composite floors with notched connections. *Eng. Struct.* **2022**, *262*, 114354. [CrossRef]
24. Sebastian, W.M.; Bell, O.G.A.; Martins, C.; Dias, A.M.P.G. Experimental evidence for effective flexural-only stiffnesses to account for nonlinear flexural-slip behavior of timber-concrete composite sections. *Constr. Build. Mater.* **2017**, *149*, 481–496. [CrossRef]
25. Ishaquddin, M.S. Gopalakrishnan. Differential quadrature-based solution for non-classical Euler-Bernoulli beam theory. *Eur. J. Mech. A/Solids* **2021**, *86*, 104135. [CrossRef]
26. Cannizzaro, F.; Fiore, I.; Caddemi, S.; Caliò, I. The exact distributional model for free vibrations of shear-bending multi-cracked Timoshenko beams. *Eur. J. Mech. A/Solids* **2023**, *101*, 105039. [CrossRef]
27. Gorik, A.V. Theoretical and experimental deformation parameters of composite beams with account of deplanation of cross sections in bending. *Mech. Compos. Mater.* **2003**, *39*, 57–64. [CrossRef]
28. Matsunaga, H. Interlaminar stress analysis of laminated composite beams according to global higher-order deformation theories. *Compos. Struct.* **2002**, *34*, 105–114. [CrossRef]
29. Piskunov, V.G.; Grinevitskii, B.V. Variant of an analytical shear model for the stress-strain state of heterogeneous composite beams. *Mech. Compos. Mater.* **2004**, *40*, 409–417. [CrossRef]
30. Yang, Z.; Zhu, H.; Yu, F.; Wu, P.; Fang, H. Thermo-mechanical coupled behavior of laminated beams with temperature-dependent viscoelastic interlayers. *Eur. J. Mech. A/Solids* **2023**, *100*, 105000. [CrossRef]
31. Zhang, Z.; Sun, Y.; Xiang, Z.; Qian, W.; Shao, X. Transient Thermoelastic Analysis of Rectangular Plates with Time-Dependent Convection and Radiation Boundaries. *Buildings* **2023**, *13*, 2147. [CrossRef]
32. Zhang, Z.; Zhou, D.; Zhang, J.; Fang, H.; Han, H. Transient analysis of layered beams subjected to steady heat supply and mechanical load. *Steel Compos. Struct.* **2021**, *40*, 87–100.
33. Li, X.; Wu, P.; Fang, H.; Wang, J.; Yu, Y. 3D viscoelastic solutions for bending creep of layered rectangular plates under time-varying load. *Compos. Struct.* **2023**, *325*, 117590. [CrossRef]
34. Yu, F.; Guan, B.; Wu, P.; Fang, H.; Gu, Z. Long-term behavior of multilayered angle-ply plate structures with viscoelastic interlayer by state space method. *Thin Walled Struct.* **2022**, *171*, 108766. [CrossRef]
35. Guan, B.; Xu, T.; Yue, K.; Deng, W.; Wu, P.; Zhang, J. Exact solution and case studies for composite I-beam with corrugated steel web. *Case Stud. Constr. Mater.* **2023**, *19*, e02422. [CrossRef]
36. Loehrmann, J. *Wood Handbook: Wood as an Engineering Material*; Departament of Agriculture: Washington, DC, USA, 1999; pp. 53–101.
37. Girhammar, U.A.; Gopu, V.K.A. Composite beam-columns with interlayer slip-exact analysis. *J. Struct. Eng.* **1993**, *119*, 1265–1282. [CrossRef]
38. Tao, H.; Shi, B.; Yang, H.; Wang, C.; Ling, X.; Xu, J. Experimental and finite element studies of prefabricated timber-concrete composite structures with glued perforated steel plate connections. *Eng. Struct.* **2022**, *268*, 114778. [CrossRef]